# Chapter 29

# Sediment transport

## 29.1 Introduction

The following seven test cases have been developed to illustrate the various options implemented in the sediment transport module

**bedload** Compares the different formulations for bed load transport by imposed currents (bottom stress) values (see Section 7.4).

**totload** Compares the different formulations for total load transport by imposed current (bottom stress) values (see Section 7.5).

**wavload** Compares formulations for bed and total load transport with wave effects using imposed values for currents and wave parameters (wave height, period and direction).

**sedvprof** Simulates the diffusion and settling of sediments in a water column by a bottom stress imposed via an external pressure gradient (surface slope).

**sedhprof** This test case, taken from Hjelmfelt & Lenau (1970), simulates the transition between a non-eroding and an eroding bed. This is modeled by applying a boundary condition with a concentration of zero at the upstream boundary. Note that the velocity field is supplied as an initial condition, rather than calculated by COHERENS. Both 2-D and 3-D simulations are performed and different model settings are applied to simulate the convergence to an equilibrium state.

**seddens** Simulates the evolution of an initial sediment distribution in a closed channel, consisting of vertically uniform concentrations in a section at the left of the channel and zero concentrations to the right.

The sediment is allowed to settle due to is own weight. A current is generated by the horizontal concentration gradient.

**thacker** This test case, after Thacker (1981), simulates the oscillations in a rotating parabolic basin with moving boundaries (shores lines). The oscillations generate a bottom stress by which sediments are suspended in the water column.

## 29.2 Test case *bedload*

### 29.2.1 Model setup

The aim of this test case is to compare the different formulations for bed load transport implemented in COHERENS. The simulations are performed in 0-D mode (i.e. iopt_grid_nodim=1, nz=1) without hydrodynamic calculations. A space and time independent current is imposed instead. The flow velocity takes values between 0.2 and 2 m/s with steps of 0.2 m/s. A bed roughness of 1 mm is taken.

### 29.2.2 Experiments and output parameters

The following experiments are defined

***A* :** Meyer-Peter & Müller (1948)

***B* :** Engelund & Fredsøe (1976)

***C* :** Van Rijn (1984b)

***D* :** Wu *et al.* (2000)

***E* :** Soulsby (1997)

***F* :** Van Rijn (2003)

The following output test parameters are defined

umean current [m/s]

bstres (non-normalised) bottom stress $\rho_0 \tau_b$ [Pa]

qbed bedload mass transport $\rho_s q_b$ [kg/m/s]

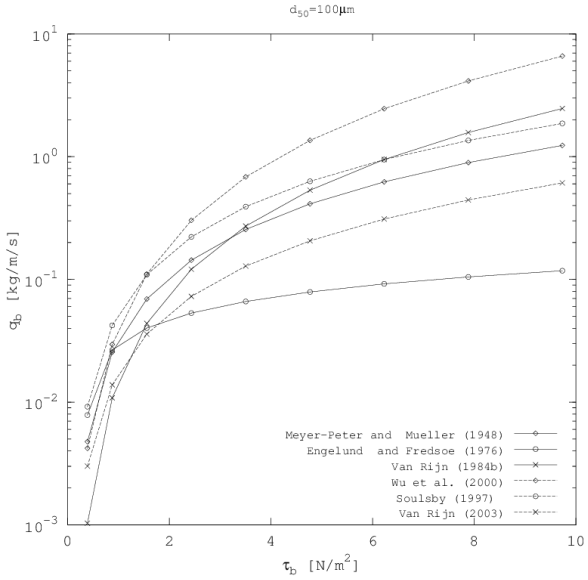


Figure 29.1: Bed load mass transport (kg/m/s) as function of the bed shear stress (Pa), using six different formulations. Characteristic grain size used for all formulas: 100$\mu$m.

### 29.2.3 Results

Results are shown in Figures 29.1–29.3 for simulations using the formulations by Meyer-Peter & Müller (1948), Engelund & Fredsøe (1976), Van Rijn (1984b), Wu *et al.* (2000), Soulsby (1997) and Van Rijn (2003). It can be seen that the computed transport rates seem to converge at some value of the flow velocity. For the cases with a grain size of 1000$\mu$m the convergence occurs near the maximum flow and shear stress, for the case with grain size 450$\mu$m near $\tau_b$ 3–4 Pa (except van Rijn 2003), but for the case with grain size 100$\mu$m that point is already reached near $\tau_b < sim2$ Pa and consequently the transport rates for higher flow velocities diverge for different formulations. Near the converging point the different formulas deviate a factor 2 to 3, while for $d = 100\mu$m at $\tau_b = 8$ Pa the range is a factor 50. The reason

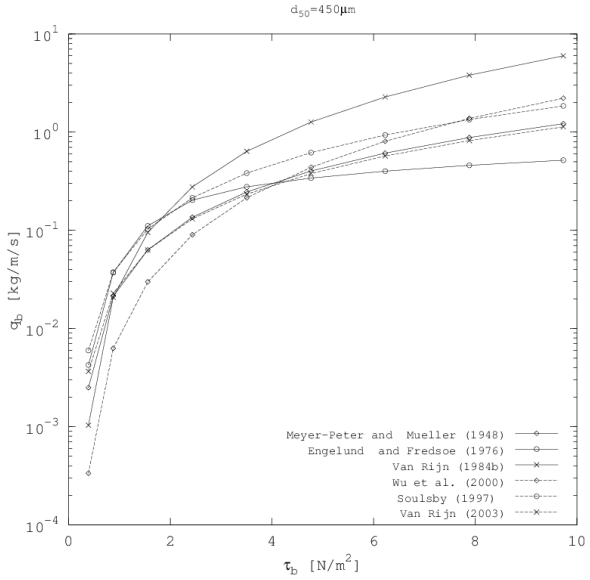


Figure 29.2: Bed load mass transport (kg/m/s) as function of the bed shear stress, using six different formulations. Characteristic grain size used for all formulas: $450\mu$.

is the large range of exponents applied to the near-bed flow velocity: from 1 in the Engelund & Fredsøe (1976) formula to 4.4 in the Wu *et al.* (2000) formula.

### 29.2.4 Conclusion

For medium to coarse sands and for fine sands under relatively low shear stress, the different formulations for bed load transport are in the same range (minimum and maximum values within factor 3 from mean). For fine sands under larger shear stress a wider range of values is obtained. This might be due to the different definition of bed load transport used during measurements of bed load and the development of bed load transport in the sediment model (e.g. maximum level above the bed). This becomes more apparent for

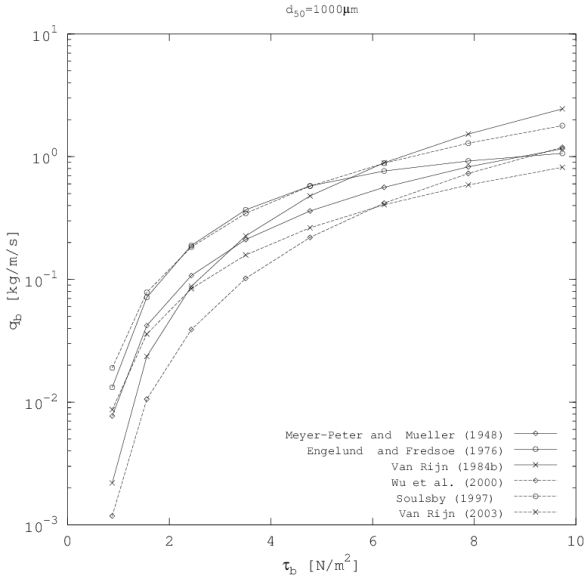


Figure 29.3: Bed load mass transport (km/m/s) as function of the bed shear stresss, using six different formulations. Characteristic grain size used for all formulas: 1000$\mu$m.

fine materials under high shear stress. It is advised to use a either compatible suspended load equation (or total load formulation) or the combination with an advection-diffusion solution for suspended load in this case.

The validity range of transport formula is an important issue, for example, the Engelund & Fredsøe (1976) was calibrated on sands with minimum diameter of 190$\mu$m. Indeed, we see that this formula deviates strongly for fine sands. The only formula for experiments on fine sands ($d_{50} \leq 100\mu$m) is the one by Wu *et al.* (2000). Even though the Meyer-Peter & Müller (1948) formula was developed for gravel only, its results are always in the centre of the range of values computed by the different formulae.

## 29.3 Test case *totload*

### 29.3.1 Model setup

This test case compares different formulations for bed load transport. Setup is the same as for test case ***bedload*** using an imposed current which varies between 0.2 and 2 m/s and a bed roughness of 1 mm.

### 29.3.2 Experiments and output parameters

The following experiments are defined

***A*** **:** classic form of the Engelund & Hansen (1967) formula

***B*** **:** Engelund & Hansen (1967) using the Chollet & Cunge (1979) expression for $\theta_*$

***C*** **:** Ackers & White (1973)

***D*** **:** Wu *et al.* (2000)

***E*** **:** Van Rijn (2003)

***F*** **:** Van Rijn (2007a)

The following output test parameters are defined

vmean current [m/s]

bstres (non-normalised) bottom stress $\rho_0 \tau_b$ [Pa]

qtot total load mass transport $\rho_s q_t$ [kg/m/s]

### 29.3.3 Results

From Figures 29.4–29.6, showing computations of total load transport with the formulas of Engelund & Hansen (1967), Chollet & Cunge (1979), Ackers & White (1973), Wu *et al.* (2000), Van Rijn (2003) and Van Rijn (2007a), it is clear that for total load the different formulae give a more narrow band of transport rates compared to the bed load only formulations, except for the Chollet & Cunge (1979) formula. The widest variation is still computed for the very fine sands of $d_{50} = 100\mu$m.

Due to the addition of suspended load to the bed load component, the Van Rijn (2003, 2007a) formulations differ slightly due to the different formulation of turbulence damping. This effect is more pronounced in the fine sands computations since the lower Rouse number leads to more suspension.

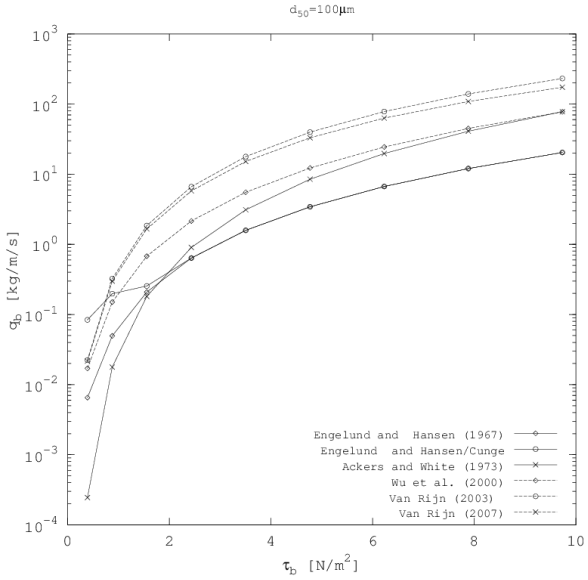


Figure 29.4: Total load mass transport (kg/m/s) as function of the bed shear stress (Pa), using six different formulations. Characteristic grain size used for all formulas: 100$\mu$m.

A remark should be given about the original Engelund & Hansen (1967) formulation and the one using the Chollet & Cunge (1979) extension. In the former only sheet flow conditions have been considered, while in the latter the different transport regimes have been taken into account. As can be seen from the results, the Chollet & Cunge (1979) relationship deviates from the former in conditions where sheet flow is least expected: on coarse grained beds and at low bed shear stress. For coarse sand ($d_{50}$ = 1mm) it is clear that the Chollet & Cunge (1979) formula results in transport rates up to a magnitude higher. For medium sands ($d_{50}$ = 450$\mu$m) it still shows higher transport rates, up until a bed stress of 8 Pa where both curves converge. For fine sands ($d_{50}$ = 100$\mu$m) both equations are identical for a bed stress of 2.5 Pa or above. The user should be aware of these differences.

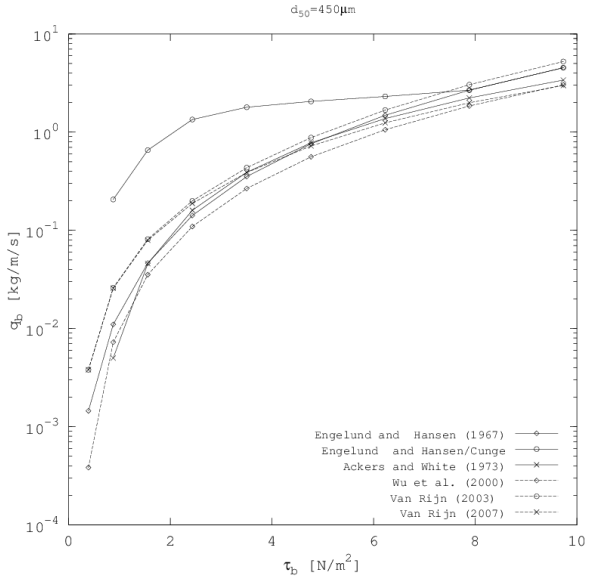


Figure 29.5: Total load mass transport (kg/m/s) as function of the bed shear stress (Pa), using six different formulations. Characteristic grain size used for all formulas: 450$\mu$m.

### 29.3.4 Conclusion

The user should be aware that the formulation of Chollet & Cunge (1979) predicts considerably higher transport rates than all other formulae for coarse sediment and/or low flow velocity. Considering the six different equations, the minimum and maximum transport rates obtained are within a factor 2 larger or smaller than the average, except for the original Chollet & Cunge (1979) equation. It is strongly recommended to keep the switch iopt_sed_eha at the value of one.

It should be considered by the user that the formulation of Wu *et al.* (2000) makes of use a fixed formulation for critical shear stress (inherent to the formula) which cannot be changed by the user. However, when using the recommended values based on the Shields curve in the other total load

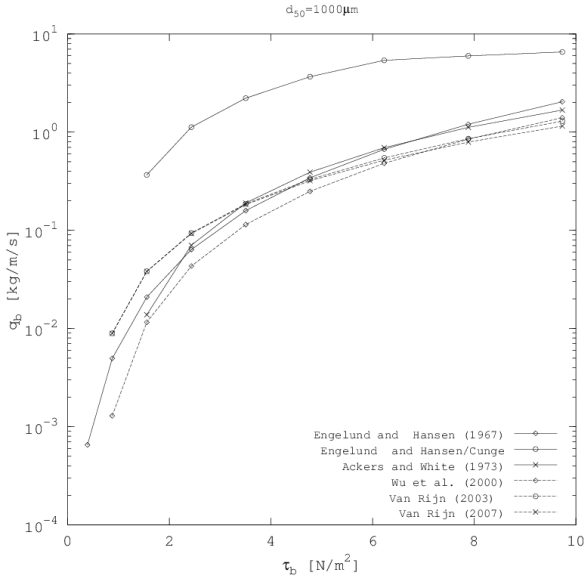


Figure 29.6: Total load mass transport (kg/m/s) as function of the bed shear stress (Pa), using six different formulations. Characteristic grain size used for all formulas: 1000$\mu$m.

formula results are very similar.

## 29.4 Test case *wavload*

### 29.4.1 Model setup

The set up of this test case is the same as for tests ***bedload*** and ***totload***. In order to conduct primary tests to verify the impact of waves on the load formulae, the uniform and steady current field, imposed in the same way as in the previous tests, is now combined with a range of wave heights, periods and directions.

Wave height $H_s$ varies from 0.05 to 5.0 m, wave periods from 4 to 11 s and

the angle between current and waves from -90 to 90 degrees (with intervals od 22.5 degrees), i.e. from waves traveling perpendicular to the current direction as to waves traveling in the same direction as the current. Each experiment is made using 10 different currents, 10 wave heights (and periods) and 9 wave directions, a total of 900 simulations is performed for each experiment.

A total roughness length of 1 mm has been used in all simulations, but it should be noted that for the wave part of the bed shear stress most formulae use the grain roughness length since it is assumed that the form roughness is not important for small wave boundary layers and wave orbital excursions in the order of 1 m. For all computations a grain size of 250 $\mu$m has been used.

### 29.4.2 Experiments and output parameters

The following experiments are defined

***A*** **:** Soulsby (1997)

***B*** **:** Madsen & Grant (1976)

***C*** **:** Van Rijn (2003)

***D*** **:** Van Rijn (2007a)

The following output test parameters are defined

| | |
|---|---|
| umean | current [m/s] |
| bstres | (non-normalised) bottom stress $\rho_0 \tau_b$ [Pa] |
| wheight | wave height [m] |
| wperiod | wave period [s] |
| wdir | wave direction [degrees] |
| qloadmag | bed or total load mass transport $\rho_s q_t$ [kg/m/s] |
| qloaddir | bed or total load mass transport direction [degrees] |
| qbedu | bed load mass transport in the X-direction $\rho_s q_{b1}$ for experiment ***A*** [kg/m/s] |
| qbedv | bed load mass transport in the Y-direction $\rho_s q_{b2}$ for experiment ***A*** [kg/m/s] |
| qtotu | total load mass transport in the X-direction $\rho_s q_{b1}$ for experiments ***B,C,D*** [kg/m/s] |
| qtotv | total load mass transport in the Y-direction $\rho_s q_{b2}$ for experiments ***B,C,D*** [kg/m/s] |

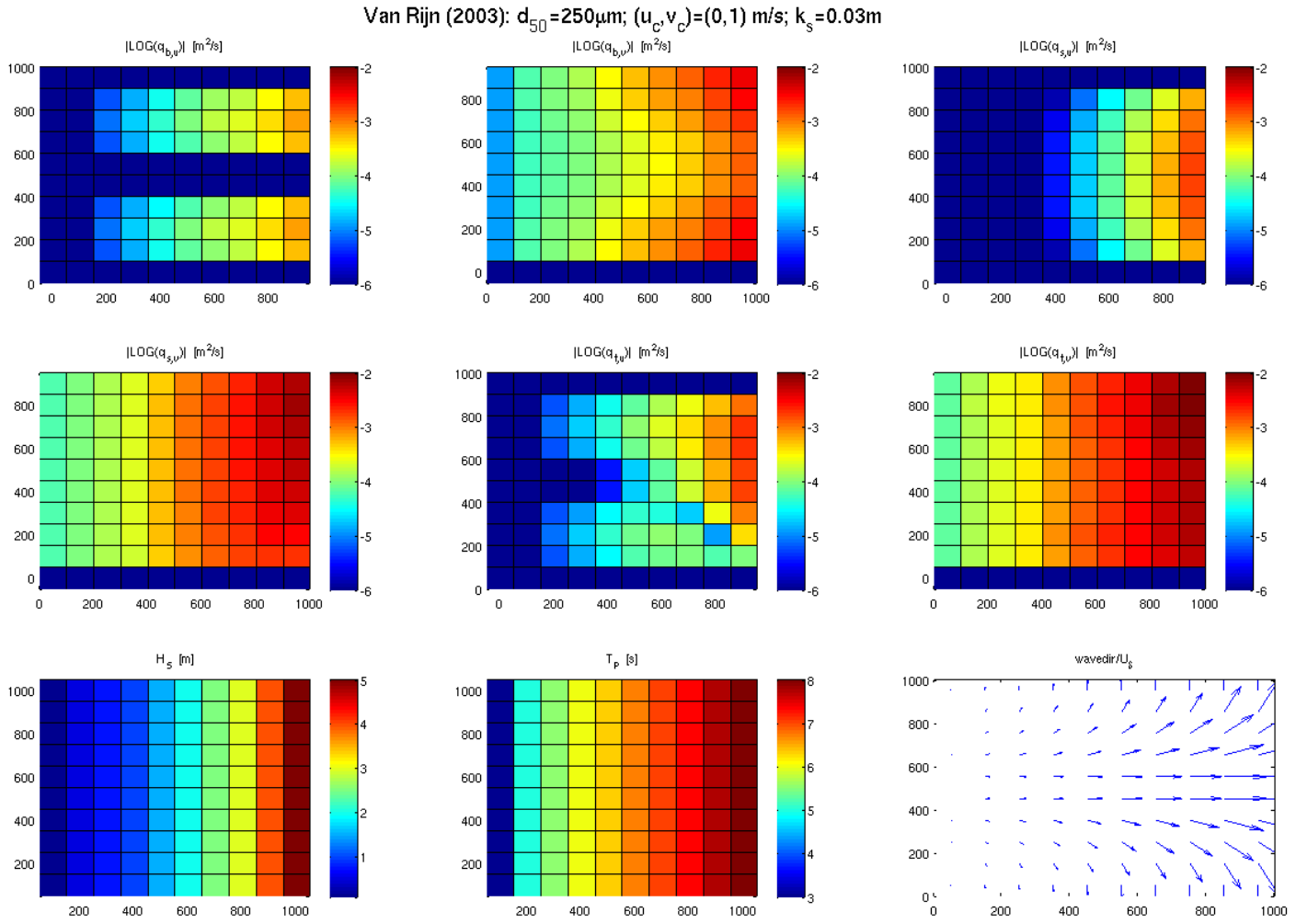


Figure 29.7: Computed bed load, suspended load and total load transport under varying wave height and direction; VR=van Rijn. Color bars indicate LOG of absolute value, except for $H_S$ and $T_P$. From left to right, and from top row to bottom row: X-component of BL, Y-component of BL, X-component of SL, Y-component of SL, X-component of TL, Y-component of TL, input $H_S$, input wave period $T_w$ and vectors of peak orbital velocity in wave propagation direction.

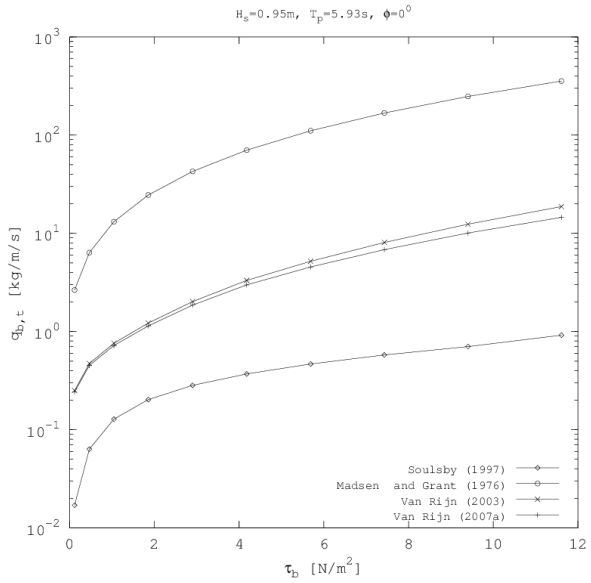


Figure 29.8: Bed/total load transport [kg/m/s] as function of the bed shear stress (Pa), $H_s$=0.95 m, $T_w$=5.92 s and $\phi_w$=$0^0$ and four different formulations.

### 29.4.3 Results

A qualitative example of the distribution of X- and Y-components of bed load (BL), suspended load (SL) and total load (TL) transport is shown in Figure 29.7. Peak orbital velocity vectors in wave propagation direction are shown below right. Input significant wave height and peak wave period is shown in the left and centre lower panels. Ambient current velocity is 1 m/s in the X-direction (East) in all cases. The influence of wave height on sediment transport is clearly visible, but also the influence of wave direction on the transport component perpendicular to the current.

Bed (experiment ***A***) and total (experiments ***B,C,D*** load transports are plotted in Figures 29.8–29.11 as function of bottom stress for two different wave heights and three different wave directions. The curves are qualita-

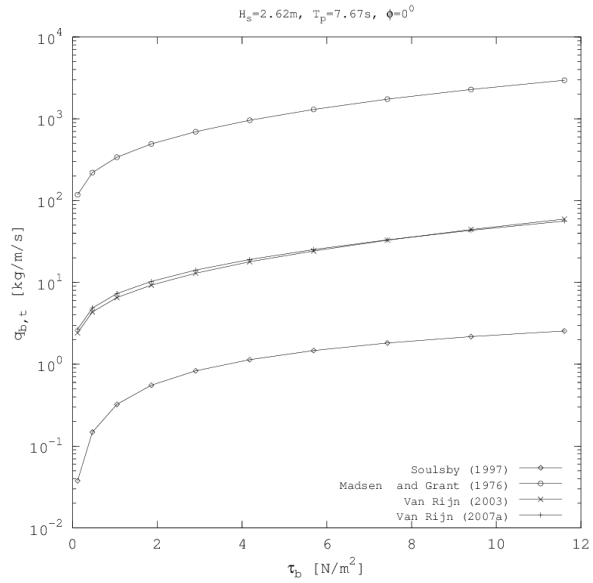


Figure 29.9: As Figure 29.8 now using $H_s$=2.62 m, $T_w$=7.67 s.

tive the same for the four experiments, but differ quantitatively. The two Van Rijn (2003, 2007a) formulations produce almost the same results whereas the Madsen & Grant (1976) values are higher by a factor 10–50 and the Soulsby (1997) lower by a factor 10. Wave direction is less significant than wave height. The highest impact occurs for $\phi_w$=45$^0$, the lowest for $\phi_w$=90$^0$.

Load transports as function of wave height are plotted in Figures 29.12–29.15 for two different bottom stresses and the same three wave directions. The dependency on $H_s$ is clearly the greatest for the Madsen & Grant (1976) case (up to a factor of 100 to 1000), followed by Van Rijn (2003, 2007a) (factor 10) and Soulsby (1997) (factor less than 10).

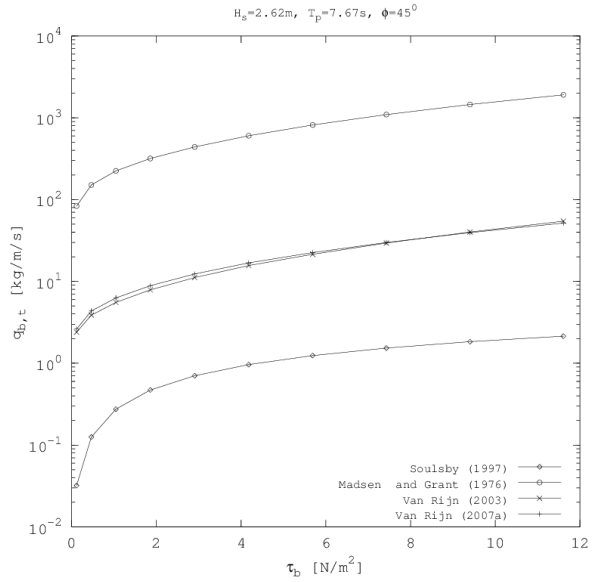


Figure 29.10: As Figure 29.9 now using $\phi_w$=$45^0$.

## 29.5 Test case *sedvprof*

### 29.5.1 Introduction

The objective of this test case is to assess the ability of COHERENS to simulate suspension transport by performing 1DV (water column) simulations. Computed longstream velocity and sediment concentration profiles are plotted against the analytical law of the wall and Rouse profile, respectively, given by

$$u = \frac{u_*}{\kappa} \ln(z/z_0) \tag{29.1}$$

$$\frac{c\,(z)}{c_a} = \left( \frac{H-z}{z} \frac{a}{H-a} \right)^{\frac{w_s}{\kappa u_* \beta}} \tag{29.2}$$

where $u$ is the longstream velocity, $\kappa$=0.4 von Karman's constant, $u_*$ the bed shear velocity given by $\sqrt{\tau_b/\rho_w}$ with $\tau_b$ the bed shear stress and $\rho_w$

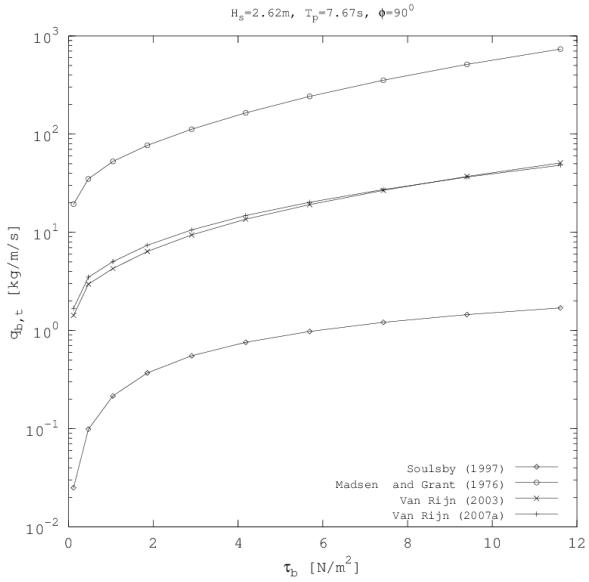


Figure 29.11: As Figure 29.9 now using $\phi_w$=$90^0$.

the water density, $z_0$ is the bed roughness coefficient, $c\,(z)$ the suspended sediment concentration, $c_a$ the equilibrium sediment concentration near the bed at reference level $a$, $w_s$ the settling velocity and $\beta$ the ratio of the sediment diffusion coefficient to the momentum diffusion coefficient (inverse of the Prandtl-Schmidt number).

### 29.5.2 Model setup

A quadratic formulation of the critical bed shear stress is adopted, with a spatially uniform bed roughness $z_0$ set to 0.001 m, $d_{50} = 250\mu m$ and $\rho_s = 2650kg/m^3$. An equilibrium bed shear velocity $u_*$ is imposed through a surface slope using $u_* = \sqrt{g\partial\zeta/\partial x} = 0.07$ m/s. The settling velocity $w_s$ is set to a constant value. Fluid density is considered as uniform, i.e. without sediment contributions. The model settings are summarized in Table 29.1

Simulations are performed for multiple values of the ratio $u^*/w_s$ – i.e.

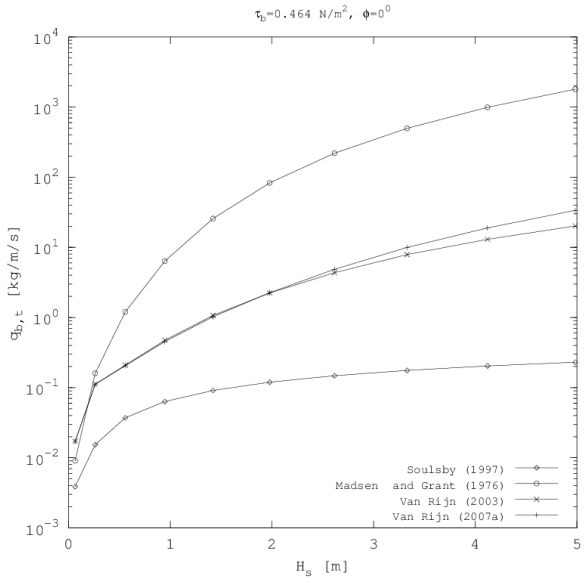


Figure 29.12: Bed/total load transport [kg/m/s] as function of wave height, $\phi_w$=$0^0$ and $\overline{u}$=0.4 m/s ($\tau_b$=0.464 N/m$^2$).

low settling velocity $u_*/w_s = 10$, medium settling velocity $u_*/w_s = 5$ and high settling velocity $u_*/w_s = 1$ – and two formulas for the bed boundary condition – i.e. Van Rijn (1984b) and Smith & McLean (1977). In addition, the influence of the vertical grid resolution on result accuracy is tested by carrying out simulations with 5, 10, 15, 25, 50, 100 and 200 vertical grid layers, non-uniformly distributed over the water height (higher resolution at the bed).

All simulations are performed in 1DV mode (iopt_grid_nodim=1) with a water depth of 10 m. A parabolic profile is taken for sediment diffusion (see equation (4.154)). The initial current is set to zero.

$$D_V = \kappa H u_* \frac{z}{H}\left(1 - \frac{z}{H}\right) \tag{29.3}$$

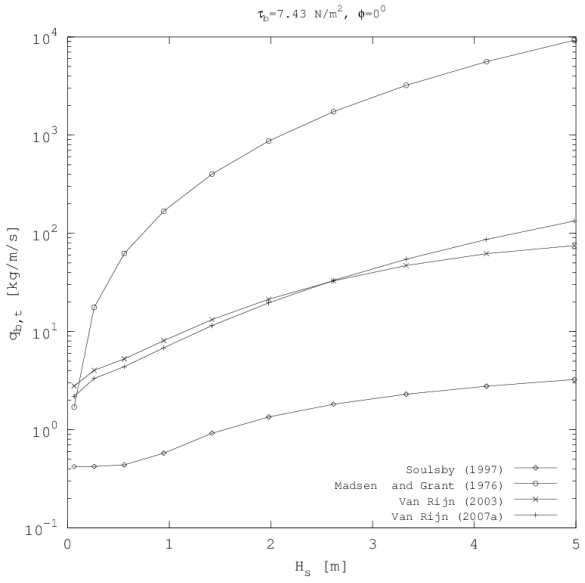


Figure 29.13: As Figure 29.12 now for $\overline{u}$=1.6 m/s ($\tau_b$=7.43 N/m$^2$).

### 29.5.3 Results

Figure 29.16 plots the theoretical law of the wall of equation (29.1) against the velocity profile calculated by COHERENS, and this for the different vertical grid resolutions.

As described in the model setup, simulations were performed for three values of the parameter $u_*/w_s$. Figures 29.17 and 29.18 plot the theoretical Rouse profile against the simulated results, with the formula of Smith and McLean and Van Rijn employed as bed boundary condition, respectively.

The suspended sediment transport concentration profiles for $u_*/w_s = 10$ and $u_*/w_s = 1$ are displayed in Figures 29.19 and 29.20, respectively. The bed boundary condition of Smith and McLean was retained for these simulations.

Since an accurate determination of the net sediment transport at the bed is essential to the calculation of bed deformation and, thus, channel morphology, it is prudent to evaluate the performance of COHERENS in

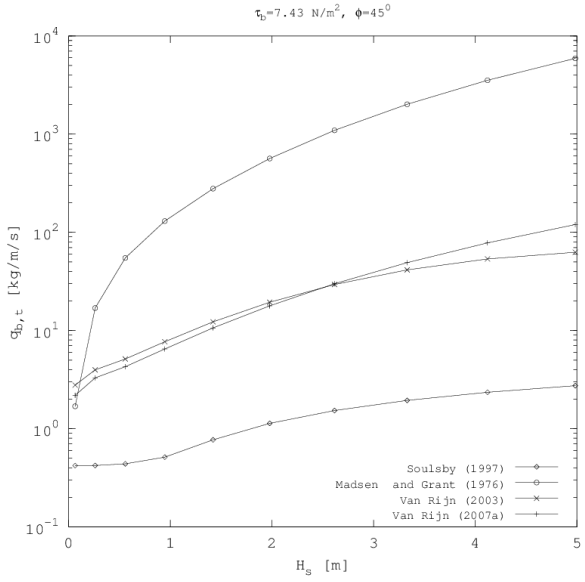


Figure 29.14: As Figure 29.13 now for $\phi_w$=$45^0$.

balancing sediment deposition and erosion fluxes through the bed with the amount of sediment in suspension. The difference of these two terms should be zero for mass conservation (or sufficiently small to be deemed negligible). Figure 29.21 shows the temporal evolution of the net deposition and erosion flux through the bed, indicating that, indeed, the channel has reached a state of equilibrium and that the total amount of suspended sediment at the final time step can be compared to the sediment transport flux through the bed, integrated over time. Table 29.2 displays this comparison for different values of the vertical grid resolution.

### 29.5.4 Conclusions

- COHERENS approximates the theoretical longstream velocity profile very well. While increasing the vertical grid resolution improves accuracy for the lower vertical grid resolutions, this improvement becomes

Table 29.1: Model setup for suspended sediment concentration test cases

| Characteristic | Model setting |
|---|---|
| Vertical grid resolution | 5, 10, 15, 25, 50, 100, 200 layers |
| Water depth | 10 m |
| Hydrodynamics | Enabled |
| Turbulence formulation | Parabolic |
| Initialisation | zero flow, zero turbulence, zero suspended sediment |
| $D_{50}$, $\rho_s$, $z_0$ | 200$\mu$m, 2650 kg/m$^3$, 0.001 m |
| Bed shear stress | quadratic |
| Critical bed shear stress | Brownlie (1981) |
| Bed boundary condition | Van Rijn (1984a) or Smith & McLean (1977) |
| Settling velocity | $w_s$=0.007, 0.014, 0.07 m/s |
| Density | Uniform |
| Time step | 12 s |
| Simulated time | 12 h |

Table 29.2: Comparison of total amount of suspended sediment with total net transport through the bed

| | Vertical grid resolution | | | | | | |
|---|---|---|---|---|---|---|---|
| Parameter | 5 | 10 | 15 | 25 | 50 | 100 | 200 |
| Net sediment transport through bed [m$^3$] | 3.5624 | 3.8012 | 3.9127 | 4.0278 | 4.1456 | 4.2298 | 4.2891 |
| Volume of suspended sediment [m$^3$] | 3.5624 | 3.8012 | 3.9128 | 4.0278 | 4.1457 | 4.2298 | 4.2895 |
| Difference [%] | $< 10^{-3}$ | $< 10^{-3}$ | 0.0026 | $< 10^{-3}$ | 0.0024 | $< 10^{-3}$ | 0.0093 |

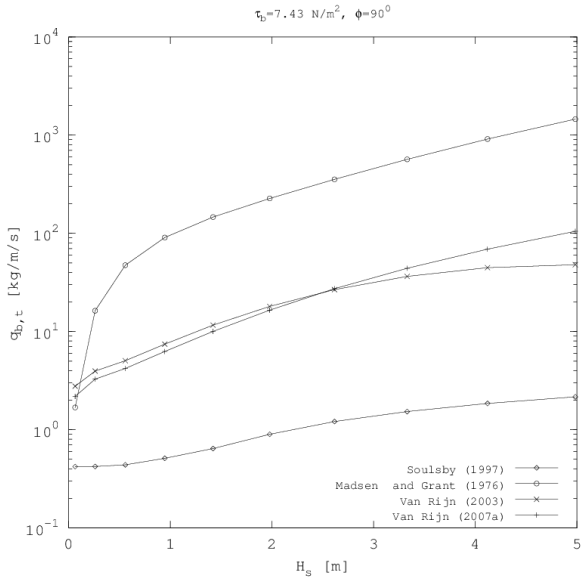


Figure 29.15: As Figure 29.13 now for $\phi_w$=$90^0$.

negligible from 50 layers onwards.

- There is a very good agreement between the theoretical Rouse profile and the simulated results for $u_*/w_s$=5 and $u_*/w_s$=10, while some inaccuracy occurs for $u_*/w_s$=1. This could be attributed to the high concentration gradient that occurs near the bed in cases of high settling, which – even with the TVD scheme – introduces numerical diffusion into the model and in turn causes the computed concentrations to be higher than they are in reality. Nevertheless, considering that the numerical results are displayed on a logarithmic scale, the margin of error is reasonable. The lack of data points in the direction of the water surface in the nz=5 and nz=10 curves indicates that $c = 0$ for these points, an expected approximation error when employing low vertical resolutions in cases with high settling velocity.

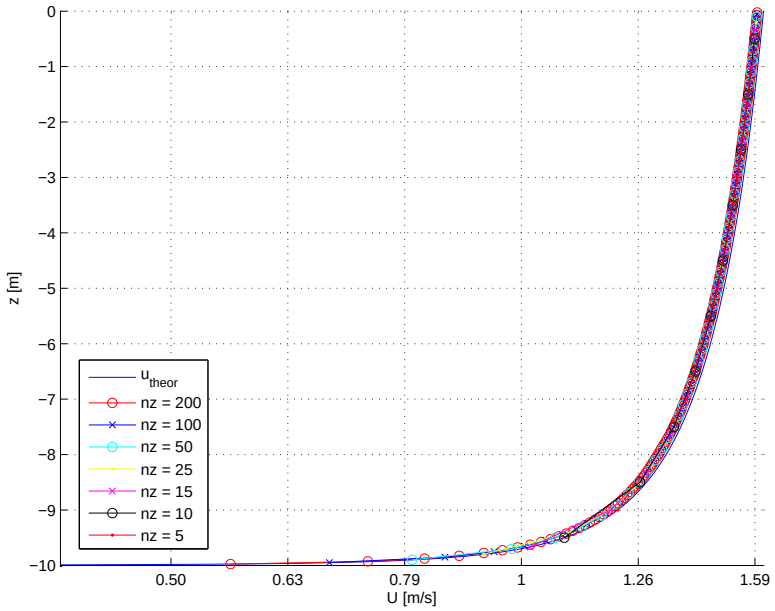


Figure 29.16: Velocity profile versus the theoretical law of the wall

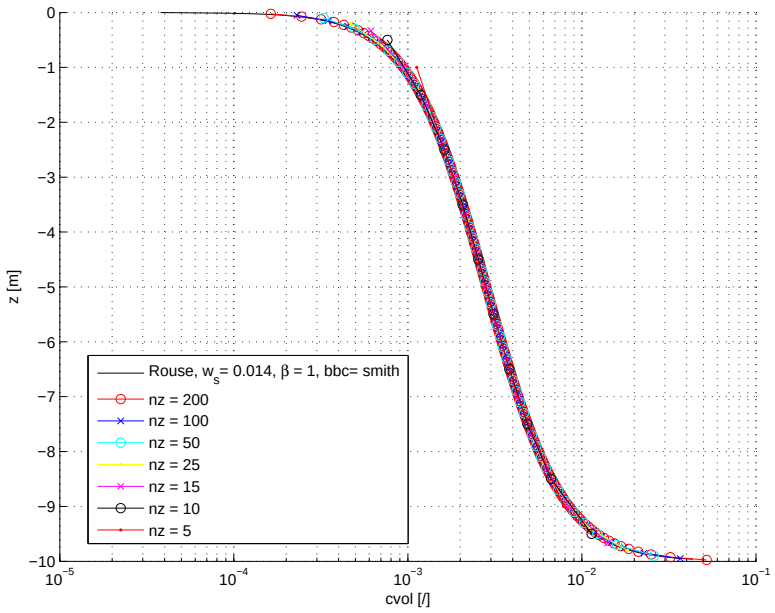


Figure 29.17: Suspended sediment concentration profile versus the theoretical Rouse profile for $u_*/w_s = 5$ and bed boundary condition of Smith & McLean (1977)

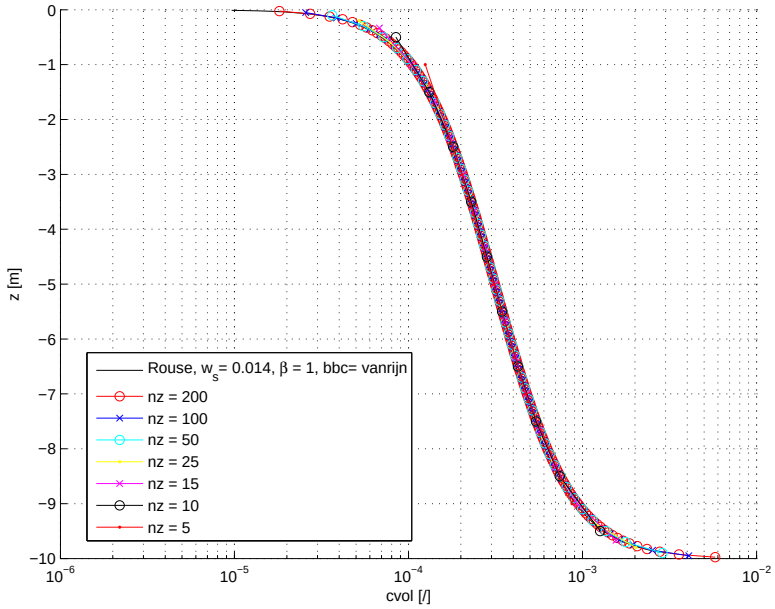


Figure 29.18: Suspended sediment concentration profile versus the theoretical Rouse profile for $u_*/w_s = 5$ and bed boundary condition of Van Rijn (1984a)

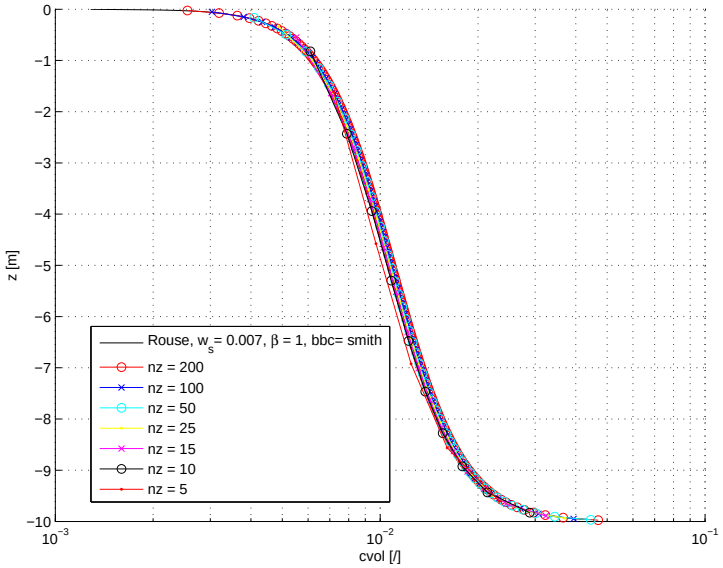


Figure 29.19: Suspended sediment concentration profile versus the theoretical Rouse profile for $u_*/w_s = 10$

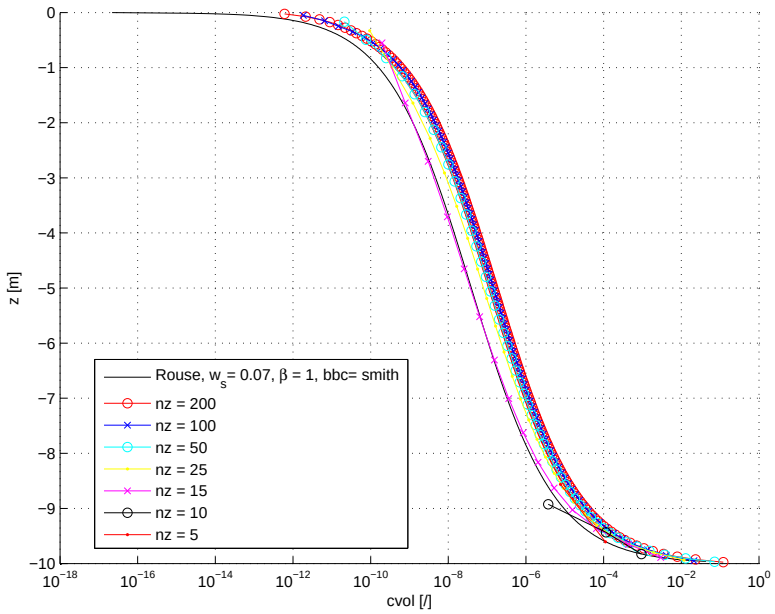


Figure 29.20: Suspended sediment concentration profile versus the theoretical Rouse profile for $u_*/w_s = 1$

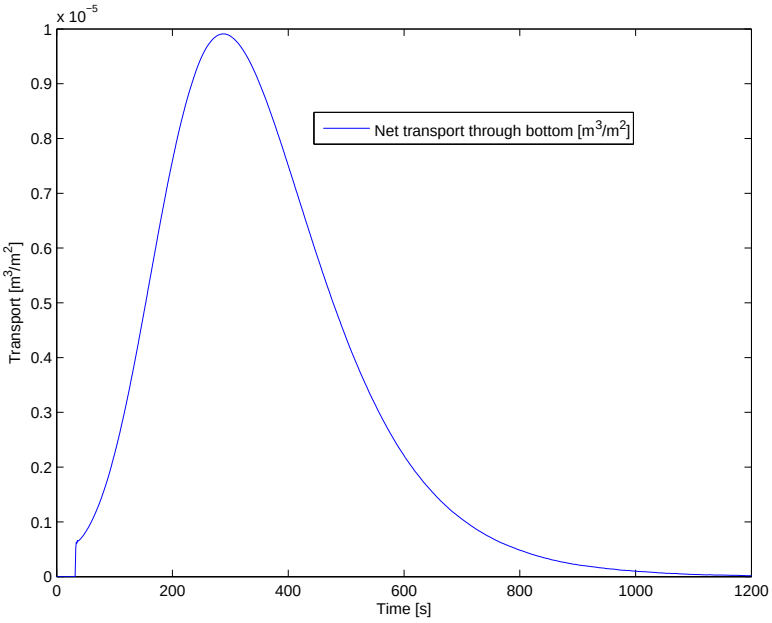


Figure 29.21: Temporal evolution of the net sediment transport flux through the bed (nz=50 layers)

Table 29.3: Settings of the switches for the ***sedvprof*** experiments.

| switch | ***A*** | ***B*** | ***C*** | ***D*** | ***E*** | ***F*** | ***G*** | ***H*** |
|---|---|---|---|---|---|---|---|---|
| nz | 50 | 200 | 200 | 200 | 200 | 200 | 200 | 200 |
| iopt_sed_ws | 1 | 1 | 1 | 1 | 2 | 4 | 5 | 1 |
| iopt_sed_taucr | 2 | 2 | 2 | 3 | 2 | 2 | 2 | 2 |
| iopt_sed_bbc | 1 | 1 | 2 | 1 | 1 | 1 | 1 | 1 |
| iopt_sed_beta | 1 | 1 | 1 | 1 | 1 | 1 | 1 | 3 |

- Table 29.2 shows a perfect agreement between the calculated total net sediment transport through the bed in time and the total amount of suspended sediment particles at equilibrium. An increase in vertical grid resolution yields a significant increase in both quantities for resolutions smaller than 50 layers, showing the importance of the grid resolution with respect to bed morphology calculations. At higher resolutions, this increase becomes negligible. Figure 29.21 shows a logical evolution of the net sediment transport through the bed from the initiation of motion up to the equilibrium state. The calculated value for the flux at equilibrium equals 1.22 $10^{-9}$ (or ca. 4cm/year), which is negligible.

### 29.5.5 Experiments and output parameters

Different settings of sediment switches can be compared by the user through a number of additional experiments and *.tst* files provided to the user. Specific definitions are listed in Table 29.3.

The following output test parameters are defined

| | |
|---|---|
| umean | depth-mean current [m/s] |
| ubot | bottom current [m/s] |
| usur | surface current [m/s] |
| refconc | reference concentration [$m^3/m^3$] |
| heightc | (non-dimensional) reference height |
| bsed_flux | bottom sediment flux [$m^3/s/m^2$] |
| sedbot | bottom concentration [$m^3/m^3$] |
| sedmin | minimum concentration over the vertical [$m^3/m^3$] |
| sedmax | maximum concentration over the vertical [$m^3/m^3$] |
| sedint | vertically integrated concentration [$m^4/m^3$] |

## 29.6 Test case *sedhprof*

### 29.6.1 Introduction

In this test case, the development of a suspended sediment concentration which starts at the transition between a non-erodible and an erodible bed is simulated. For this situation, an analytical expression for the sediment concentration profiles as a function of the distance from the transation was derived by Hjelmfelt & Lenau (1970). Only for the special case that $u_*/w_s = 5$, the analytical expression takes a simple form, with elementary functions only. The dimensionless sediment concentration, $\hat{c} = c/c_a$, is expressed as a function of the dimensionless terms $X = \frac{\beta\kappa u_* x}{\overline{u}H}$, $Z = z/H$ and $A = z_a/H$ where $\overline{u}$ is the depth-averaged flow velocity. This results for this situation in:

$$\hat{c} = \sqrt{\frac{A}{1-A}}\sqrt{\frac{1-Z}{Z}} + \frac{\sqrt{A}}{\sqrt{Z}\sin^{-1}\sqrt{1-A}}\sum_{K=1}^{\infty}\frac{(-1)^K\,\alpha_K \sin\left[2\alpha_K \sin^{-1}\sqrt{1-Z}\right]}{\left(\alpha_K^2 - \frac{1}{4}\right)}e^{-X\left(\alpha_K^2 - 1/4\right)} \tag{29.4}$$

with

$$\alpha_K = \frac{K\pi}{2\sin^{-1}\sqrt{1-A}} \quad \text{for} \quad K = 1, 2, 3, ... \tag{29.5}$$

In this solution, it was assumed that the velocity field is constant in space and time (also over the depth), while the eddy-diffusivity has a parabolic shape:

$$D_V = \beta\kappa z u_* \left(1 - \frac{z}{H}\right) \tag{29.6}$$

Here, $\kappa$ is the Von Kármán's coefficient, $\beta$ the ratio of the sediment diffusion coefficient to the momentum diffusion coefficient (inverse of the Prandtl-Schmidt number).

The objective of this test case is to compare the results of two-dimensional sediment transport (using an equilibrium concentration and an adaptation time scale) with a complete three-dimensional simulation and different available formulations to calculate the equilibrium concentration for two-dimensional sediment transport.

### 29.6.2 Model setup

In order to perform a simulation that can be easily compared with the analytical solution, the flow field and diffusivity are given as initial conditions

Table 29.4: Overview of model setup

| Simulation | 2D | 3D |
|---|---|---|
| nc | 3 | 3 |
| nr | 121 | 121 |
| nz | 1 | 30 |
| $\Delta t$ [s] | 10 | 10 |
| $u_*$ [m/s] | 0.03 | 0.03 |
| $H$ [m] | 10 | 10 |
| $d_p$ [$\mu$m] | 89.48 | 89.48 |
| $w_s$ [mm/s] | 6.0 | 6.0 |

and the fixed values of these parameters are used in a simulation, in which only sediment concentrations are calculated.

Thus no simulation of the hydrodynamics is performed. The transition between a non-erodible and erodible bed is simulated by applying an upstream boundary condition for the sediment concentration of 0 $m^3/m^3$. All simulations are run starting from a zero initial concentration towards a stable equilibrium. Six simulations were performed, 6 in 2-D and one in 3-D (30 layers). An overview of the setup conditions is given in Table 29.4.

### 29.6.3 Experiments and output parameters

A number experiments each using a different formulation for the equilibrium concentrations are defined. All experiments, except the last one, are performed in 2-D.

***A*** **:** Using the depth-averaged Rouse profile (7.128) and 7 points for Gauss-Legendre quadrature.

***B*** **:** As ***A*** now using 3 points for vertical integration.

***C*** **:** Using (7.129) and the Engelund & Hansen (1967) formulation for suspended load.

***D*** **:** Using (7.129) and the Ackers & White (1973) formulation for suspended load.

***E*** **:** Using (7.129) and the Van Rijn (2003) formulation for suspended load.

***F*** **:** Using (7.129) and the Wu *et al.* (2000) formulation for suspended load.

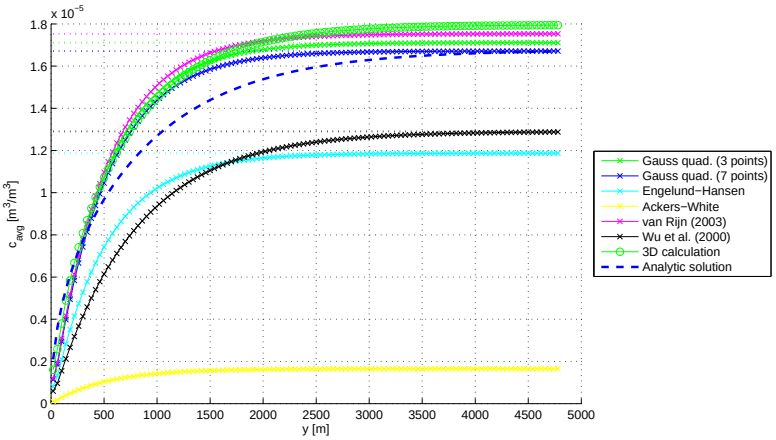


Figure 29.22: Depth averaged concentration as function of distance from the boundary (for different sediment transport models). Equilibrium concentrations are shown with a dotted line.

***G*** **:** As experiment ***A*** now in 3-D mode.

Output test parameters are

| | |
|---|---|
| sedmin | minimum concentration over the horizontal [$m^3/m^3$] |
| sedmax | maximum concentration over the horizontal [$m^3/m^3$] |
| sedint | horzontally integrated concentration at the bed [$m^4/m^3$] |
| time_scale | distance where the sediment concentration has grown to 0.99 of its maximum value |
| e_scale | distance where the sediment concentration decayed by a factor $e$ with respect to its maximum value |

### 29.6.4 Results

In Figure 29.22, the depth averaged concentration is shown as function of the distance from the boundary, together with the equilibrium concentration calculated by COHERENS (for the two-dimensional simulations) and the analytical solution. For the three-dimensional simulations, the calculated concentration profiles at different distances from the boundary are plotted together with the analytical solution in fig. 29.23.

### 29.6.5 Conclusion

- The results of the 2-D and 3-D simulations compare well with each other at least for the Gaussian quadrature with seven points. The equilibrium

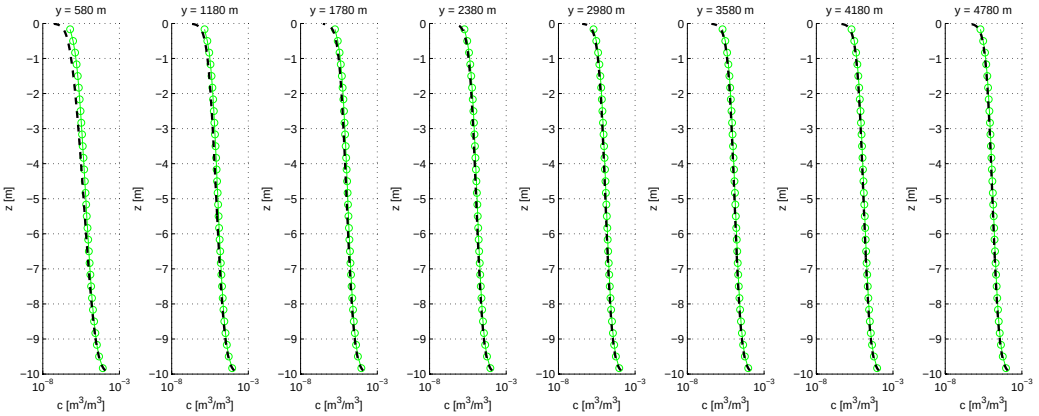


Figure 29.23: Calculated sediment concentration profiles (3D calculation; green) and analytical solution (black).

concentration is better approximated in 2-D than in 3-D. The reason is that with 30 cells, the resolution near the bed is still not high enough in 3-D to capture the concentration profile well. For the 2-D simulation(s), it seems that seven cells are sufficient for the Gaussian quadrature, while the equilibrium concentration is overestimated slightly with three cells.

- The length scales needed for the adaptation in the 2-D and 3-D simulations compare well. This agrees with the fact that the 3-D case was used to determine the 2-D parameterisation for the adaptation time scale. The adaptation lengths in the model solutions are somewhat smaller than the one from the analytical solution.

- The concentration profiles in the 3-D simulation compare well with the analytical solution. The difference in the first observation point are strongly exaggerated by the use of a logarithmic scale for the concentration.

- The model of Van Rijn (2003) for the equilibrium situation gives similar results as the use of the Rouse profile of the 3-D simulation. This could have been expected, because the equation was derived from the same advection-diffusion approach.

- The models of Engelund & Hansen (1967) and Wu *et al.* (2000) give equilibrium concentrations that are 30% lower than the advection diffusion approach.

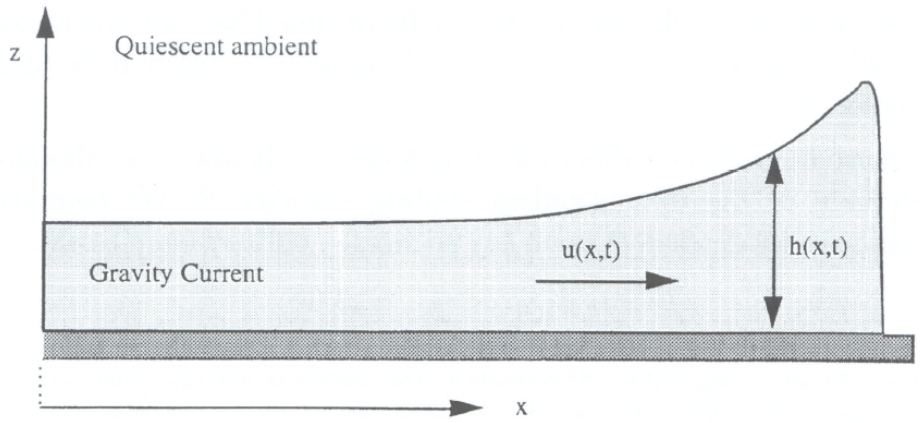


Figure 29.24: Schematic picture of a particle-laden gravity current flowing along a horizontal boundary, under a deep and otherwise quiescent ambient fluid (Hogg *et al.*, 2000).

- The model of Ackers & White (1973) gives equilibrium concentrations that are an order of magnitude lower than the other models.
- The concentrations obtained from the different formulations for the equilibrium concentration (low values for Ackers & White (1973), similar values for Engelund & Hansen (1967) and Wu *et al.* (2000)) agree with the findings for the total load test case ***totload*** (see section 29.3) for the present conditions (small $d_p$ and $u_*$).

## 29.7 Test case *seddens*

### 29.7.1 Introduction

Particle-driven gravity currents arise whenever suspensions of heavy particles are released into an ambient fluid. Because of the presence of the particles, the density of the suspension differs from that of the ambient, and a buoyancy force is induced which drives the flow. Figure 29.24 displays a schematic picture of such a particle-driven gravity current.

The objective of this test case is to assess the ability of COHERENS to simulate density-driven gravity currents. The test case setup is based on the findings of Hogg *et al.* (2000), who derived an asymptotic extension to the classic similarity solution for a theoretical 2-D test case in which an initial volume of sediment creates a density current in the longitudinal direction, while sediment particles settle downward out of the gravity current.

Table 29.5: Model setup for ***seddens*** test case

| Characteristic | Model setting |
|---|---|
| model grid | 2DV, nc=41, nr=2, $\Delta x = 0.2m$ |
| vertical grid resolution | 500 layers (uniform) |
| water depth | 10 m |
| hydrodynamics | enabled |
| turbulence formulation | k-$\epsilon$ model |
| initialisation | zero current |
| $d_{50}$ , $\rho_s$, $z_0$ | 250 $\mu$m, 2650 kg/m$^3$, 0.001 m |
| initial concentration (first meter from the left boundary) | 0.05 m$^3$/m$^3$ |
| settling velocity | $w_s$=4.5 $10^{-3}$ m/s |
| critical shear stress | $\tau_{cr}$=10 m$^2$/s$^2$ |
| density effects | enabled |
| time step | 0.01 s |
| simulated time | 10 s |

### 29.7.2 Model setup

The gravity current is simulated in a straight (2DV) channel. To facilitate comparison with the similarity solution of Hogg *et al.* (2000), the water column depth is set to 10 m and the simulation starts with a vertically homegeneous concentration of 0.05 m$^3$/m$^3$ over the five cells from the left boundary (total distance of 1 m) and is zero elsewhere. Due to the high water column to density current height ratio, a relatively high vertical grid resolution of 500 layers was chosen in order to maintain a high enough number of computational cells in the region of interest. There is no erosion of sediment at the bed (i.e. the critical shear stress $\tau_{cr}$ is set to the high value of 10 m$^2$/s$^2$), yet the calculation of sediment deposition from the gravity current onto the bed is enabled. Since the similarity solution is only valid for small settling velocities and time spans, $w_s$ was set to be 4.5 $10^{-3}$ m/s and the total time of simulation is 10 s. The model settings are summarized in Table 29.5.

### 29.7.3 Experiments and output parameters

A number experiments each using a different formulation for sinking velocity are defined.

***A*** **:** constant value of $w_s$ = 1.0E-08 m/s

***B*** **:** constant value of $w_s$ = 0.00498 m/s

***C*** **:** Camenen (2007) formulation for sand

***D*** **:** Stokes formula (7.40)

***E*** **:** Soulsby (1997)

To reduce computational costs, a reduced number of 50 vertical cells is taken.

Output parameters are

| | |
|---|---|
| bstresmax | domain maximum of the bottom stress [Pa] |
| ubot | bottom current at the location where the current height has its maximum [m/s] |
| umean | depth-mean current at the location where the current height has its maximum [m/s] |
| hcurmax | maximum value of the current height, defined as the distance above the sea bed where the concentration drops below 0.01 $m^3/m^3$ [m] |
| xmax | distance from the left boundary where the current height has its maximum value [m] |
| hgradmax | domain maximum for the (horizontal) gradient of the depth-mean concentration [$m^3/m^2$] |
| sedmax | domain maximum of sediment concentration [$kg/m^3$] |
| sedmin | domain minimum of sediment concentration [$kg/m^3$] |
| sedtot | total amount of sediment in the water column [$kg/m^3$] |
| sedbot | bottom sediment concentration at the location where the current height has its maximum [$m^3/m^3$] |
| bflxtot | horizontally integrated net bottom sediment mass flux [kg/s] |

### 29.7.4 Results

The height profile of the density current (defined as the height where sediment concentration drops below 0.01 $m^3/m^3$) and the depth-averaged velocity profile as given by the similarity solution are presented in Figures 29.25 and 29.27 for time t=1 to 10 s. Their numerical counterparts are displayed in Figures 29.26 and 29.28. Results are presented for the lowest 10% of the water column. Finally, Figure 29.29 compares the cumulative proportion of sediment that has deposited out of the gravity current predicted by the similarity solution with the one predicted by COHERENS.

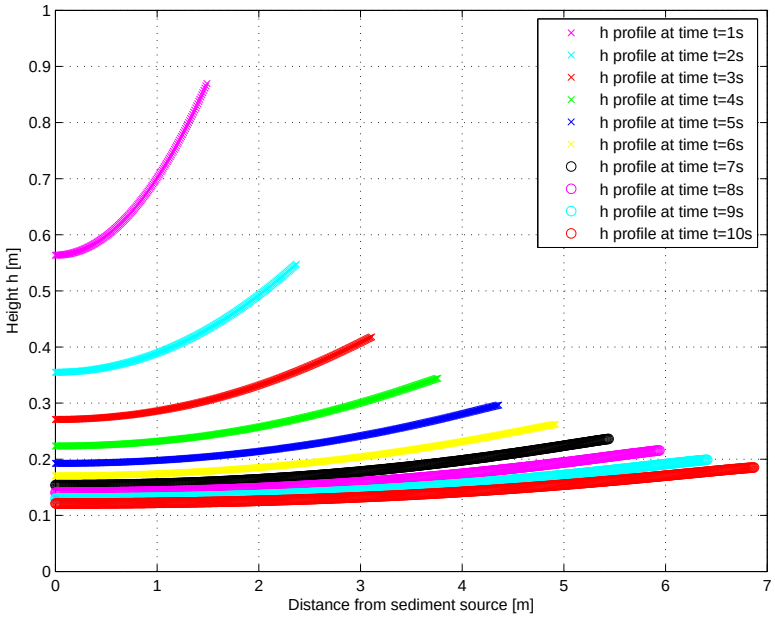


Figure 29.25: Profiles of the gravity current height derived from the similarity solution

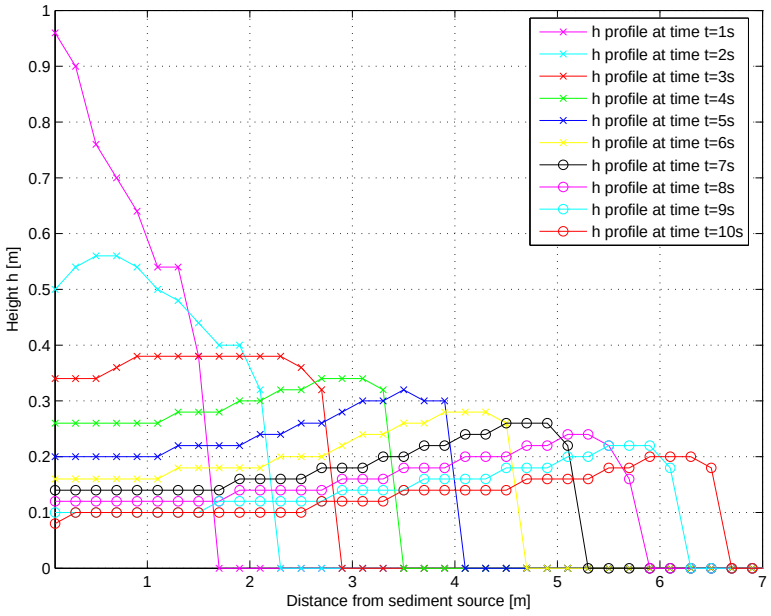


Figure 29.26: Numerical profiles of the gravity current height

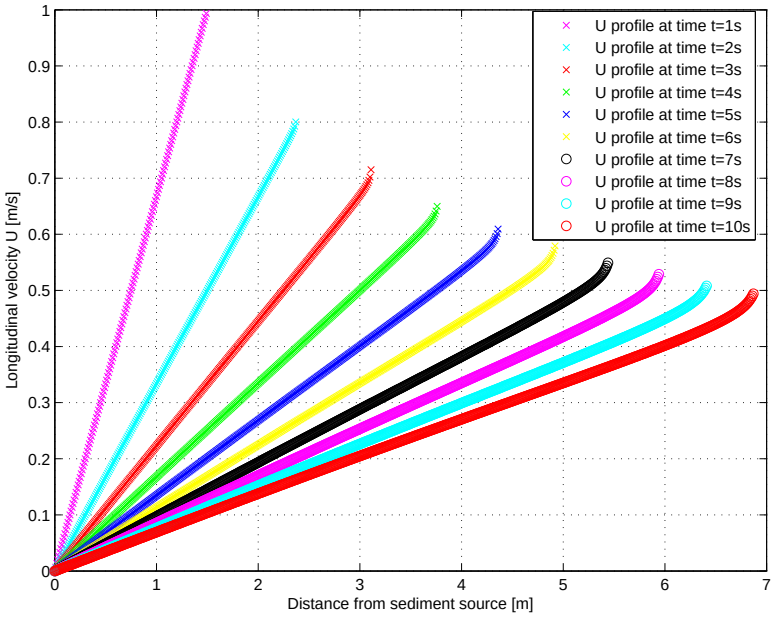


Figure 29.27: Longitudinal depth-averaged velocity profiles derived from the similarity solution

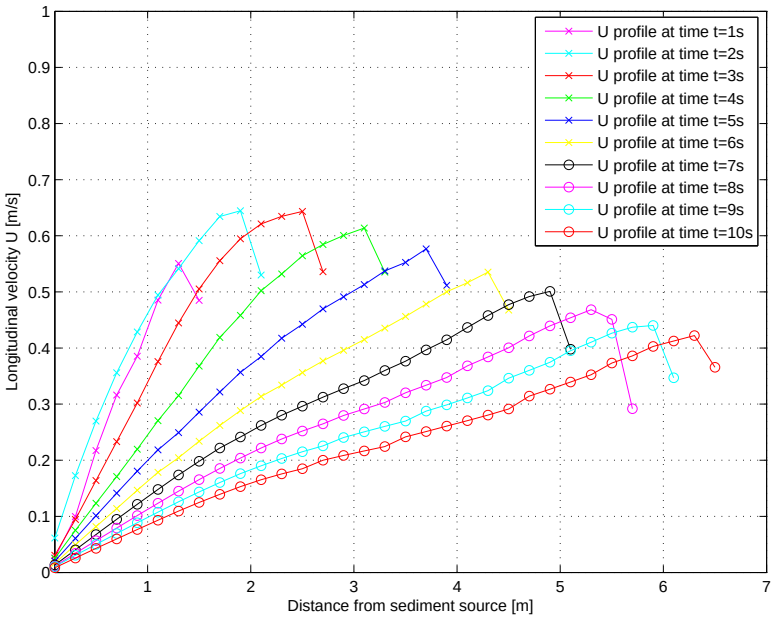


Figure 29.28: Numerical longitudinal depth-averaged velocity profiles

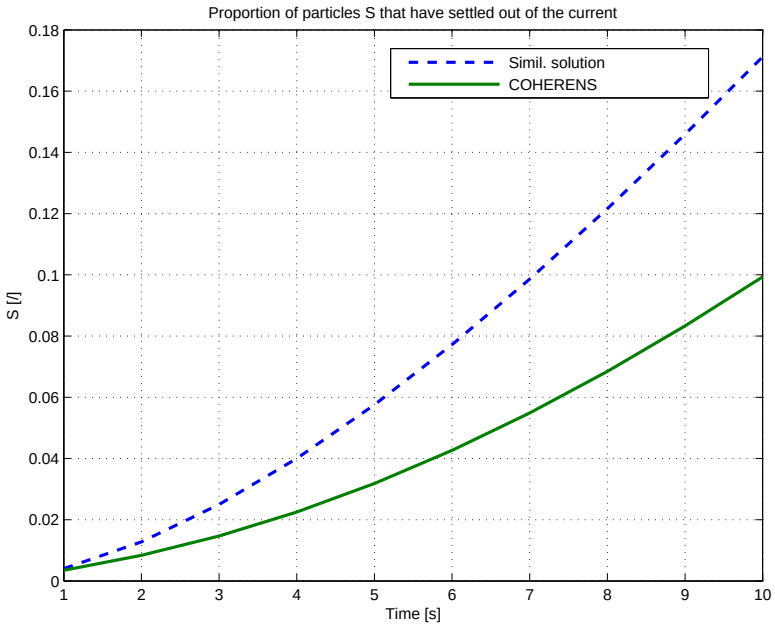


Figure 29.29: Proportion of sediment that has deposited out of the density current

### 29.7.5 Conclusion

The following conclusions can be drawn from the results presented in the previous section

- Where the position of the nose of the current is predicted accurately by COHERENS, it appears that the shape of the gravity current in the initial time steps does not agree well with the similarity solution. However, Bonnecaze *et al.* (1993) state in their paper that the propagation of a gravity current is characterised by an initial phase, during which the fixed volume of fluid collapses, before the typical shape presented in Fig. 29.24 is reached. This phase is clearly discernible in the simulated results.

- Although slightly underpredicting the values derived from the similarity solution, the velocity profiles from both solutions agree reasonably well. The large difference in the initial phase is due to the similarity solution not predicting the initial phase of current propagation, as mentioned earlier, and should therefore not be considered in the comparison.

- The evolution of the cumulative proportion of deposited sediment as calculated by COHERENS follows the same trend as the one described

by the similarity solution, yet COHERENS underpredicts the analytical results by 60 %. This is possibly due to the turbulence that keeps the sediment in the current for a longer time, and the omittance of this effect in the similarity solution.

Since it has been concluded that the initial phase of propagation predicted by COHERENS agrees with the similarity solution of Hogg *et al.* (2000) and the experimental observations of Bonnecaze *et al.* (1993), and the differences in both velocity and current height are small for later time steps, it can be concluded that the treatment of gravity currents is implemented well by the model.

## 29.8 Test case *thacker*

### 29.8.1 Introduction

The axial flow and sediment transport in a circular basin is investigated. For two-dimensional sediment transport, the analytical solutions of the hydrodynamic conditions (without friction) and sediment concentration (for non-cohesive material) are described in Pritchard & Hogg (2003) for seiches in circular and elliptical basins. For the hydrodynamics, the analytical solutions derived by Thacker (1981) are applied. The test case is based on these solutions.

The main contributions of this test case are the comparison between the hydrodynamics of the model and the analytical solution, as well as the mass conservation of the sediment in the circular basin. A comparison is made with the results of Pritchard & Hogg (2003). One should keep in mind that the comparison is not straightforward because of the non-linear bottom friction used in the model whereas the bottom stress is set to zero in the analytical solution.

### 29.8.2 Model setup

The analytical solution is described for basins which satisfy

$$h(x,y) = h_0\Big(1 - \frac{x^2}{L_x^2} - \frac{y^2}{L_y^2}\Big) \tag{29.7}$$

with $x$, $y$ the orthogonal horizontal coordinates, $h$ the mean water depth, $h_0$ the maximum depth, and $L_x$, $L_y$ the basin radii in respectively the X- and Y-direction. Figure 29.30 shows a schematic visualisation of the cross section

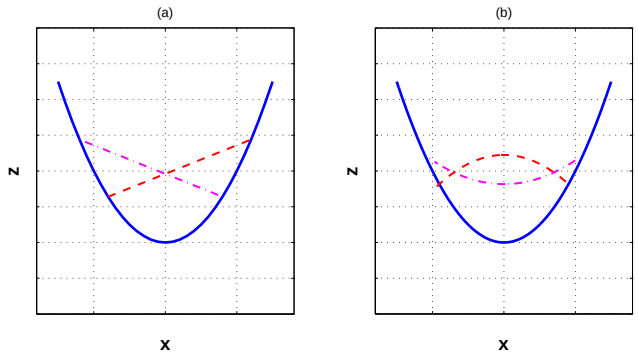


Figure 29.30: Schematic visualization of the cross sections ($y = 0$) of the basin with water level surface at two points of the oscillation (red and magenta): (a) axial mode; (b) radial mode.

of the basin with the water level surface at two points of the oscillation for the axial mode and radial mode. In the following only the axial mode will be investigated.

The analytical solution for the hydrodynamics (velocity $(u, v)$ and water level $H$) derived by Thacker (1981) are (without Coriolis force):

$$u = -\eta\omega \sin(\omega t) \tag{29.8}$$

$$v = 0 \tag{29.9}$$

$$\zeta = 2\zeta_0 \frac{h_0}{L_x} \cos(\omega t)\left(\frac{x}{L_x} - \frac{\zeta_0}{2L_x} cos(\omega t)\right) - h_0 \tag{29.10}$$

where $\omega^2 = 2gh_0/L_x^2$ and $\zeta_0$ is related to the amplitude of the surface wave.

Two cases will be considered. The first one considers a big basin (basin 1) and the second case a smaller basin (basin 2). Each grid consists of 100 grid cells in both horizontal directions. The values of the parameters are shown in Table 29.6. Hence the velocities will be small in the first basin and large in the second basin one. The simulations are performed with mud using the bottom boundary condition of Partheniades (1965) (iopt_sed_bbc = 3). The results shown are with a time step of 0.05 s and an adaptive scheme is used for the bottom flux.

### 29.8.3 Experiments and output parameters

The following experiments are defined

***A*** **:** 2-D simulation, basin 1

Table 29.6: Parameters of the problem

| parameter | unit | Basin 1 | Basin 2 |
|---|---|---|---|
| $h_0$ | m | 10 | 10 |
| $L_x = L_y$ | m | 5000 | 500 |
| $\zeta_0$ | m | 50 | 20 |
| $dp$ | m | 0.0001 | 0.00005 |
| $w_s$ | m/s | 0.001 | 0.001 |
| $\tau_{cr}$ | [kg/ms$^2$] | 0.0001 | 0.0001 |
| $\Delta t$ | s | 0.1 | 0.1 |

***B*** **:** 2-D simulation, basin 2

***C*** **:** 3-D simulation, basin 1

***D*** **:** 3-D simulation, basin 2

The following output parameters are defined

| | |
|---|---|
| bstresmean | horizontally averaged bottom stress [Pa] |
| sedmax | domain maximum of sediment concentration [m$^3$/m$^3$] |
| sedmin | domain minimum of sediment concentration [m$^3$/m$^3$] |
| sedtot | total amount of sediment in the water column [m$^3$/m$^3$] |
| bflxtot | horizontally integrated net bottom sediment mass flux [kg/s] |
| dryarea | fraction of the area which is (temporarily) dry |

## 29.8.4 Results

### 29.8.4.1 2-D simulations

1. Hydrodynamics

   - The evolution of the water level in time, together with the analytical solution at the boundary and in the middle of the basin are displayed in Figure 29.31. It shows that in the first period, the computed water level is similar to the analytical solution in the middle of the basin. Further in time they differ because of the fact that the computed solution damps out due to friction. Still the period stays the same. The water level at the boundary of the basin looks capricious, but it is small and fluctuates around zero. The vertical lines denote the time moments which are shown in Figure 29.33.

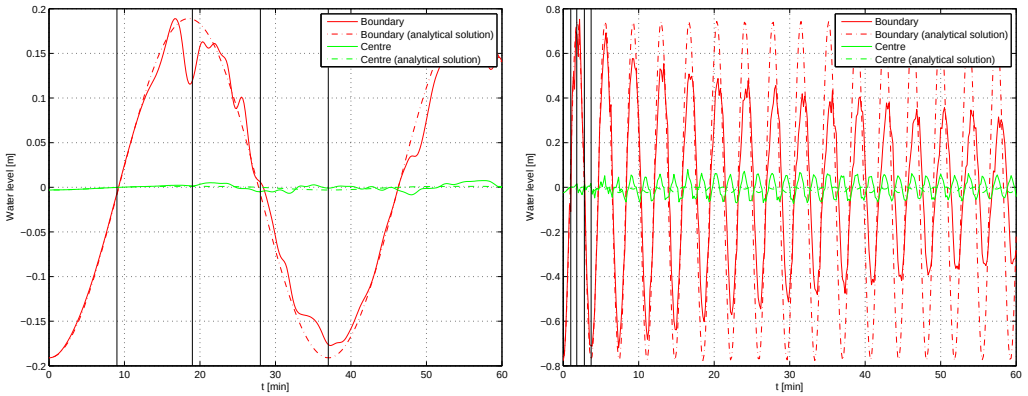


Figure 29.31: Water level in time at the boundary and the middle of the basin, together with the analytical solution for basin 1 and 2 (2-D case).

- The evolution of the velocity in time, together with the analytical solution in the middle of the basin are given in Figure 29.32. It shows that the computed velocity in the first period is similar to the analytical solution in the middle of the basin. Further in time they differ because of the fact that the computed solution damps out. Still the period stays the same. The velocity at the boundary of the basin oscillates as well, but has a reduced amplitude. The vertical lines denote the time moments which are shown in Figure 29.34.
- A profile of the water level and the velocity at different phases are displayed in respectively Figures 29.33-29.34. In the first one the water level is shown for four time steps (corresponding to the vertical lines in Figure 29.31). When the water level surface is tilted, the computed solution and the analytical resemble each other at the major part of the basin. For the flat water level surface the solution differs but note that they are both around zero. The vertical lines correspond to the boundary and the middle of the basin, visualized in Figure 29.31.

  In Figure 29.34 the velocity is shown for four time steps (corresponding to the vertical lines in Figure 29.32). When the water level surface is tilted, the velocities are at the highest and the computed and analytical solutions are comparable in the major part of the basin. For the flat water level surface the velocities are around zero, which is visible in the figure and in agreement with the analytical solution. The vertical lines correspond to the

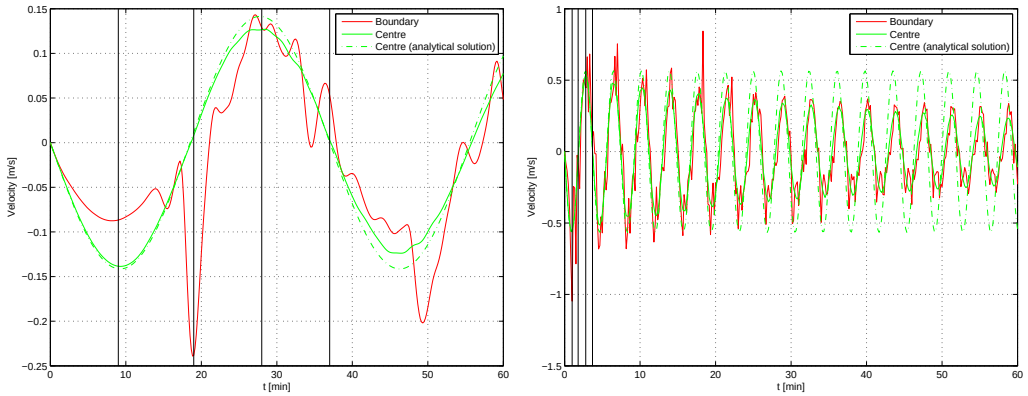


Figure 29.32: Velocity in time at the boundary and the middle of the basin, together with the analytical solution for basin 1 and 2 (2-D case).

boundary and the middle of the basin, visualized in Figure 29.32.

2. Sediment concentrations

   - A profile of the depth-averaged sediment concentration at different wave phases are shown in Figure 29.35. On the left, the sediment concentration is shown for basin 1 and is almost zero everywhere, since there is not much sediment transport due to the low currents. On the right the sediment concentration is shown for basin 2, it is constant in the middle of the basin, and has peaks on the boundaries.
   - A profile of the net bottom flux (erosion minus deposition) at different wave phases is shown in Figure 29.36. The net bottom flux for basin 1 is not displayed. There is not much sediment transport because of the low velocities, resulting in a zero net bottom flux. The net bottom flux is shown for basin 2, it is positive in the middle part of the basin and has some peaks at the boundaries.

     The case, discussed in Pritchard & Hogg (2003), is different from this case. Both cases are operating on another time scale. In the paper, the sediment is moving back and forth in the basin. In our case, due to friction, there is damping and the sediment settles quickly reaching an equilibrium. Also there is a difference in velocity at the boundary, where, in the case of Pritchard &

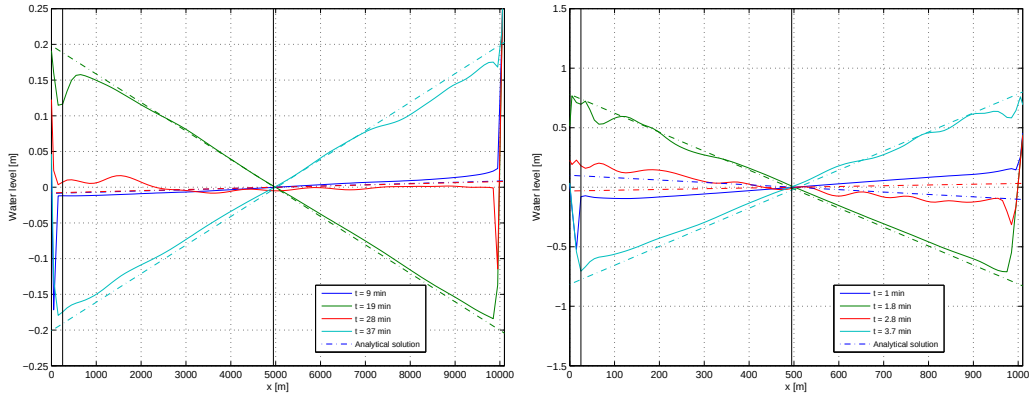


Figure 29.33: Water level at times $1/4T$, $1/2T$, $3/4T$ and $T$ where $T$ is the wave period, together with the analytical solution for basin 1 and 2 (2-D case).

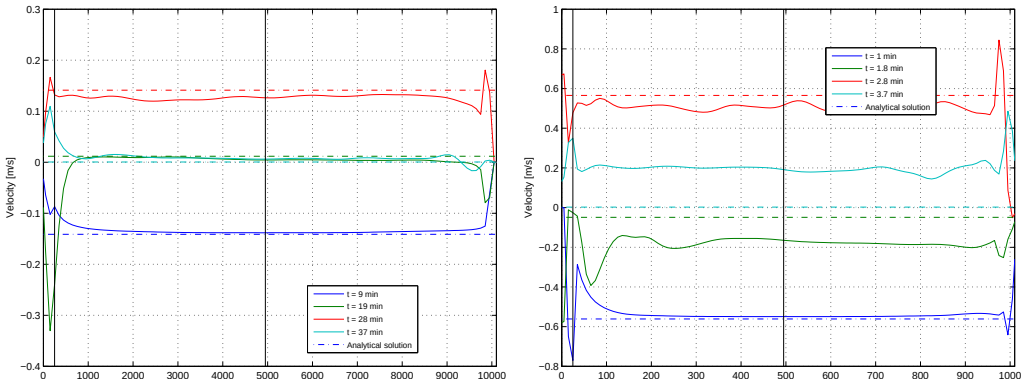


Figure 29.34: As Figure 29.33 now for the velocity.

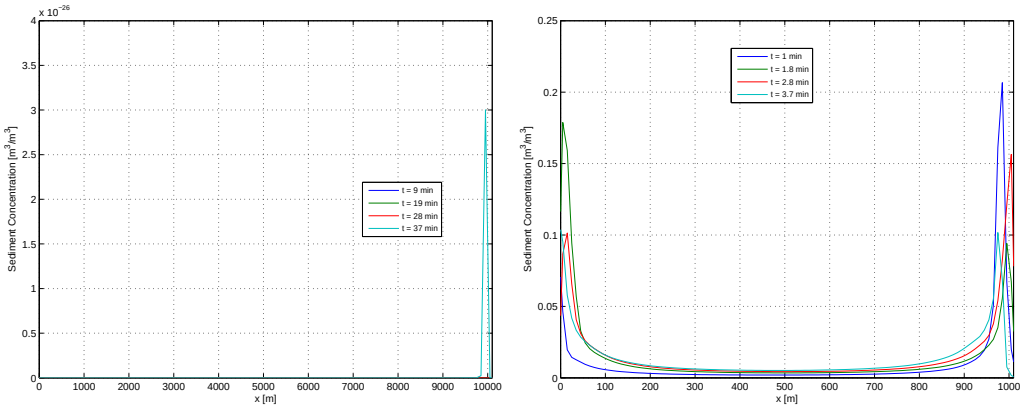


Figure 29.35: Sediment concentration at times $1/4T$, $1/2T$, $3/4T$ and $T$ where $T$ is the oscillating period for the big and small basin (2-D case).

Hogg (2003), the velocity is uniform. In our case, some velocity peaks are visible at the boundary. This has also an influence on the net bottom flux.

- The evolution of the net bottom flux (erosion minus deposition) in time at the middle of the basin is shown in Figure 29.37.
- Time series of the total volume of suspended sediment and the integral in time of the total net bottom flux are shown in Figure 29.38. It is seen that the computed values are similar, resulting in an accurate mass balance.
- The evolution of the time-averaged relative error in the mass balance as function of the time step is shown in Figure 29.39. The error decreases when the time step becomes smaller. There is a small difference between the four methods, but not really significant.
- Time series of the relative error between the total volume of suspended sediment and the integral in time of the total net bottom flux are shown in Figure 29.40. The error decrease for each time step.

### 29.8.5 3-D simulations

- A profile of the depth-averaged sediment concentration at different wave phases are shown in Figure 29.41.

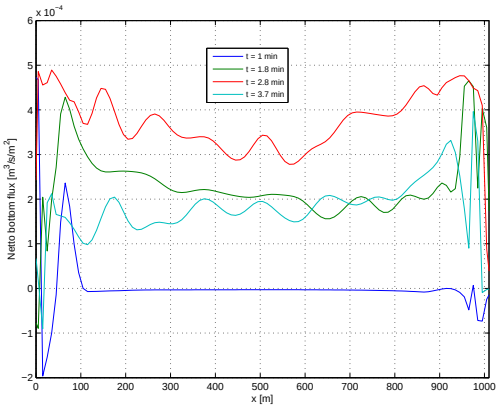


Figure 29.36: Net bottom flux at times $1/4T$, $1/2T$, $3/4T$ and $T$ for basin 2 (2-D case).

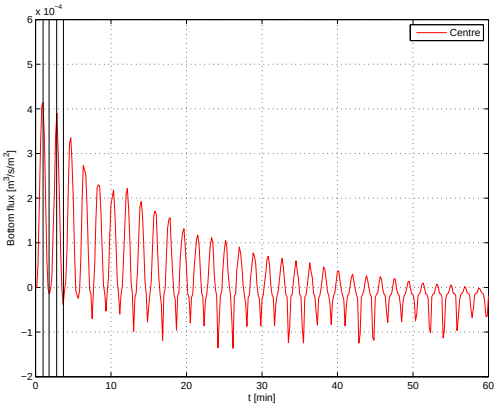


Figure 29.37: Bottom flux in time at the middle of the basin for basin 2 (2-D case).

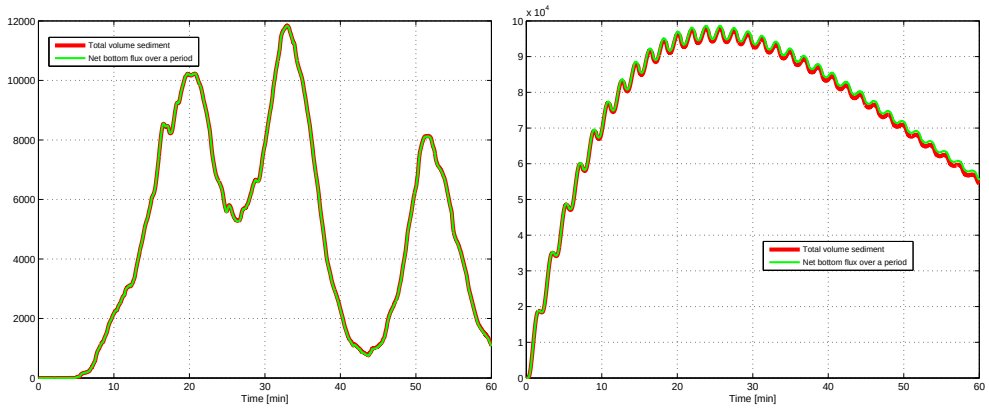


Figure 29.38: Mass balance for basin 1 and 2 (2-D case).

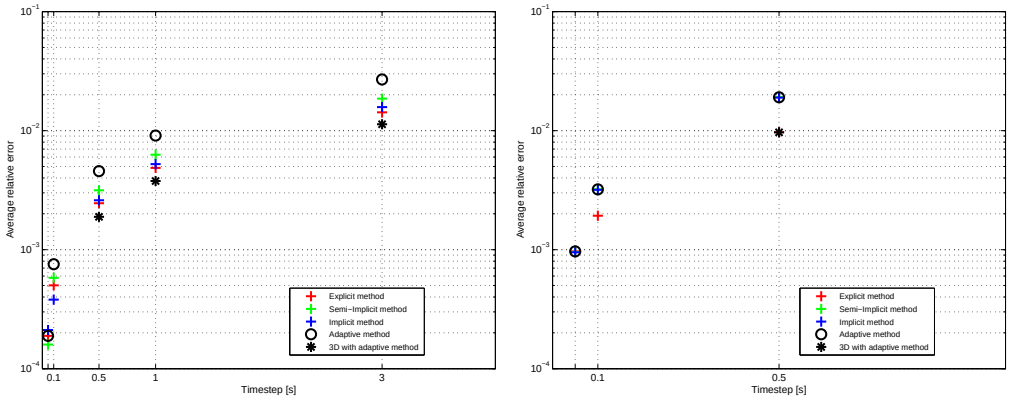


Figure 29.39: The evolution of the time-averaged error in the mass balance in function of the time step for basin 1 and 2 (2-D case).

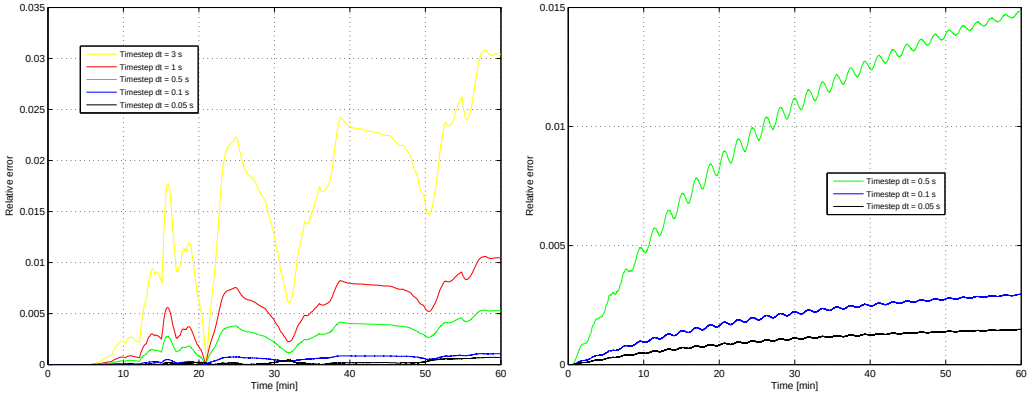


Figure 29.40: Error of mass balance in time for basin 1 and 2 (2-D case).

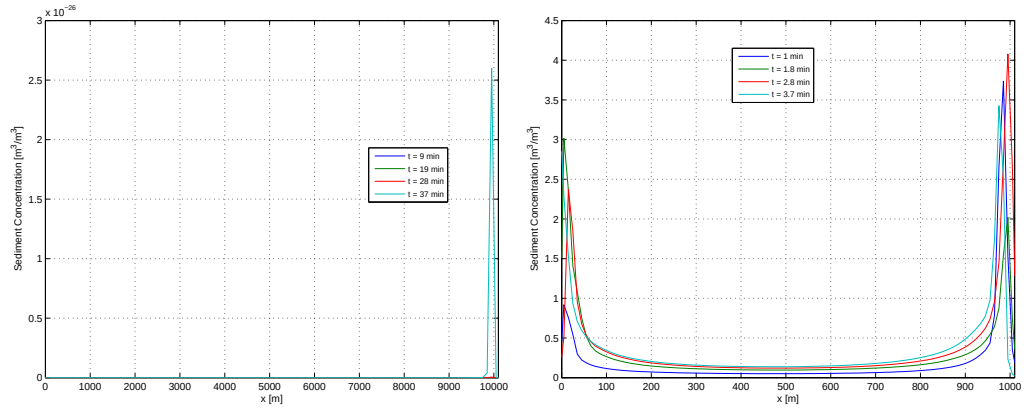


Figure 29.41: Sediment concentration at times $T/4$, $T/2$, $3T/4$, and $T$ for basin 1 and 2 (3-D case).

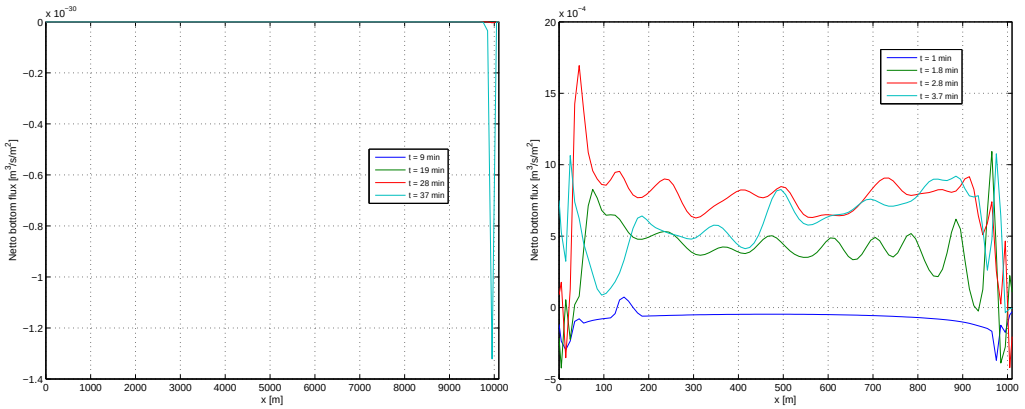


Figure 29.42: As Figure 29.41 now for the net bottom flux.

- A profile of the net bottom flux (erosion minus deposition) for different wave phases is shown in Figure 29.42.
- Time series of the total volume of suspended sediment and the integral in time of the total net bottom flux are given in Figure 29.43.
- Figure 29.44 shows the evolution of the time-averaged error in the mass balance as function of the time step.

### 29.8.6 Conclusion

This test case shows that the hydrodynamics agree well with those of the analytical solution of Thacker (1981). For the sediment, it is not possible to compare the results with Pritchard & Hogg (2003). Both problems operate on a different time scale. Nevertheless, the conservation of mass for the sediment gives accurate results. During the simulations we noticed that a small time step has to be taken, and that the sediment equation has to be solved every time step to obtain accurate results.

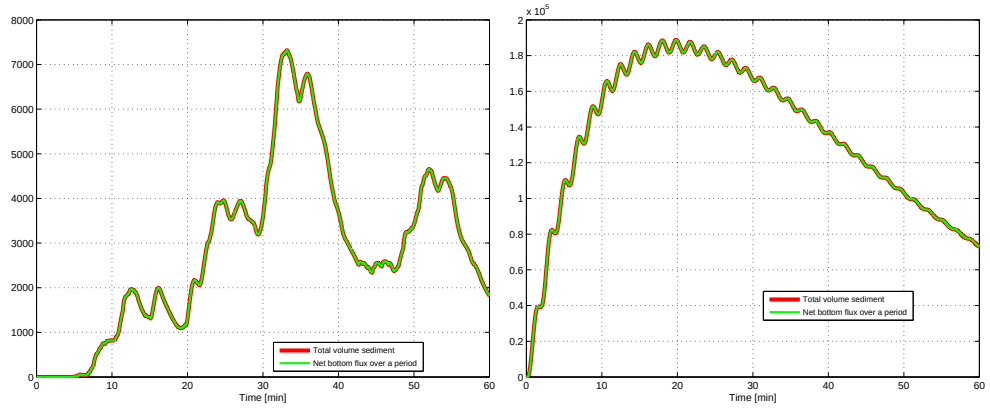


Figure 29.43: Mass balance for basin 1 and 2 (3-D case).

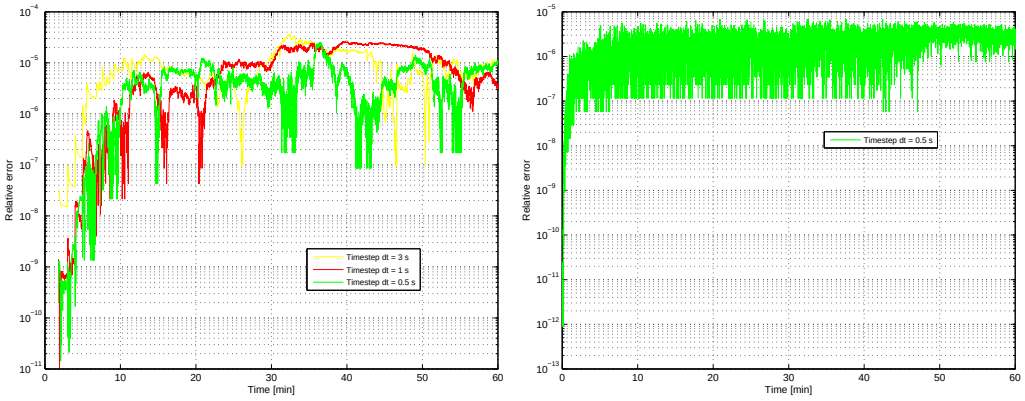


Figure 29.44: Error of mass balance in time for basin 1 and 2 (3-D case).